Probing well-characterized metal oxide surfaces with synchrotron radiation

2001 J. Phys.: Condens. Matter 13 11207

(http://iopscience.iop.org/0953-8984/13/49/308)

INSTITUTE OF PHYSICS PUBLISHING JOURNAL OF PHYSICS: CONDENSED MATTER

J. Phys.: Condens. Matter **13** (2001) 11207–11228 PII: S0953-8984(01)27904-1

Probing well-characterized metal oxide surfaces with synchrotron radiation

R Lindsay and G Thornton

Surface Science Research Centre and Chemistry Department, Manchester University, Manchester M13 9PL, UK

Received 15 August 2001
Published 10 December 2001
Online at stacks.iop.org/JPhysCM/13/11207

Abstract

The application of synchrotron radiation techniques to the study of single-crystal metal oxides has had a tremendous impact in the development of oxide surface science. This has been achieved by providing information on the electronic structure, the surface crystallography and the reactivity. In this article the major synchrotron radiation techniques applied to oxide surfaces are briefly described with the aid of examples.

(Some figures in this article are in colour only in the electronic version)

1. Introduction

For many years metal oxide substrates remained an area of minority interest within the surface science community. In part this was because of the additional complexity of metal oxides relative to metals and semiconductors, and partly because such substrates were (correctly) perceived to be more difficult to prepare and characterize. More recently, with the maturing of the field of surface science, including the emergence of scanning probe microscopes (SPM) as tools for examining surfaces at an atomic scale, interest in these important substrates has grown immensely [1]. Amongst this research activity are studies utilizing synchrotron radiation, the focus of this Special Issue of *Journal of Physics: Condensed Matter*. As will be demonstrated in this review article, the unique attributes of these photon sources have enabled significant progress to be achieved in the understanding of oxide surfaces.

In this relatively short review it is not possible to provide an exhaustive account of all the synchrotron studies on well-defined metal oxide surfaces. The approach we have adopted is to highlight examples of work performed using synchrotron radiation techniques, structured such that studies are described under technique subheadings. Our intention is to demonstrate the power of synchrotron radiation in the study of metal oxide surfaces, both clean and adsorbate covered.

2. Techniques

2.1. Photoelectron spectroscopy (PES)

Photoelectron spectroscopy (see, for example, references [2–9]) was the first synchrotron-based surface-sensitive technique to be widely applied to the study of well-characterized metal oxide surfaces. In its simplest, angle-integrating form it can be used to monitor the valence band density of states (VBDOS), fingerprint adsorbates through the position of molecular orbitals and determine core-level binding energies of the substrate and adsorbates. Employing a variable-energy photon source in the VUV and soft-x-ray region enables photoionization cross-sections to be varied, giving information on the elemental contribution to the VBDOS. It also allows the escape depth of the photoelectrons from the valence band and core levels to be varied, allowing identification of surface-related features. This can be used, for instance, to examine surface core-level shifts (SCLS) [4, 7, 8]. Resonance photoemission, which requires a tunable photon source, is discussed in the next subsection.

If the photoemission measurement is made angle-resolved (ARPES), then momentum-resolved (k-resolved) electronic structure information can be retrieved from the valence band region [2, 3, 5, 6, 9]. Here a variable-energy photon source allows $k_\perp$, the electron wave-vector perpendicular to the surface, to be varied without changing the geometry of the measurement. Angle-resolved studies of photoemission from adsorbates, in particular in combination with linearly polarized photons, can be used to determine their orientation with respect to the surface [2, 3, 5, 6, 9]. Similar measurements of core-level emission are used to record photoelectron diffraction data, which is described in subsection 2.8.

An early example of the use of synchrotron radiation photoemission to study molecular adsorption on an oxide involved water on $SrTiO_3(100)$ [10]. Results for an *in situ* fractured sample were compared with those for a sample prepared by cutting/polishing with *in situ* ion bombardment/anneal cycles. $SrTiO_3$ fractures conchoidally parallel to the (100) plane. This results in a high density of steps, which separate terraces that are SrO and TiO_2 terminated. A clear difference between the behaviours of the two types of surface was observed (see figures 1, 2). For the stepped surface, water was seen to adsorb dissociatively at room temperature to form hydroxyl species, as evidenced by the presence of only two valence band features. These correspond to emission from OHσ and OHπ occupied orbitals. For the planar surface, no adsorption was detected at room temperature, which was taken to indicate step-induced

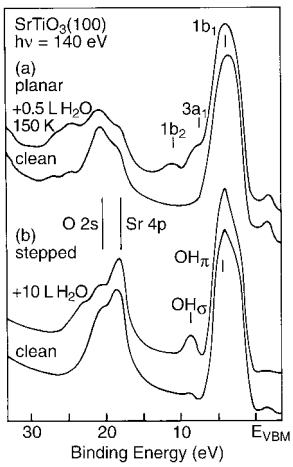

Figure 1. UPS spectra of clean and H_2O-dosed (a) planar $SrTiO_3(100)$ and (b) stepped $SrTiO_3(100)$. Exposure to H_2O was carried out with the planar surface at 150 K and the stepped surface at 300 K. (After reference [10].)

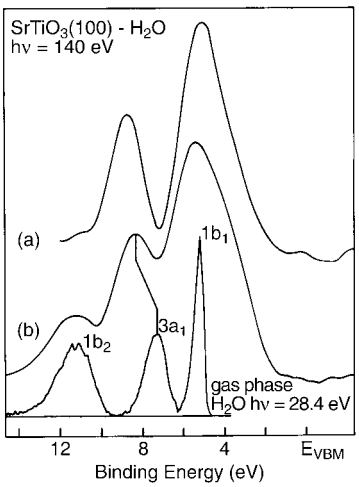

Figure 2. UPS difference spectra (H_2O dosed − clean) for (a) 10 L H_2O on stepped $SrTiO_3(100)$ adsorbed at 300 K and (b) 0.5 L H_2O on planar $SrTiO_3(100)$ adsorbed at 150 K, compared with a gas-phase photoelectron spectrum of H_2O, aligned at the $1b_2$ energy. (After reference [10].)

water dissociation. Adsorption on the planar surface was observed at 150 K. In this case three peaks are present in the valence region, corresponding to the three molecular orbitals of water. The bonding shift of the $3a_1$ peak for the adsorbed water relative to the gas phase indicates its chemisorption on $SrTiO_3(100)$.

A related study of similarly prepared $SrTiO_3(100)$ surfaces investigated SCLS phenomena [11]. For both the stepped (fractured) and the planar clean surfaces, the surface Sr 3d features lie to higher binding energy than the bulk-derived peaks by about 1 eV, while the surface Ti 3s feature is located at 1.7 eV lower binding energy. In view of the identical binding energy shifts on the two surfaces it was proposed that the SCLS features are due to surface Sr and Ti atoms occupying terrace sites. The shift of the Ti 3s surface component to lower binding energy is consistent with the expected enhancement of covalent bonding at the TiO_2-terminated surface [12]. Spectra recorded from the clean stepped surface are displayed in figure 3, along with spectra recorded following room temperature water adsorption on the same type of surface. It is known from valence band photoemission [10], discussed above, that water adsorbs dissociatively under these conditions on this surface. As can be clearly seen from figure 3, this dissociative adsorption reduces the intensity of both the Ti 3s and Sr 4p SCLS features. It was concluded that these changes are due to the formation of Sr–OH and Ti–OH surface moieties, for which the cation potentials revert back to the bulk values. For the planar surface, upon which only molecular adsorption occurs (at lower substrate temperature), water exposure depletes only the intensity of the Sr 3d SCLS component, indicating that molecular adsorption occurs only on SrO-terminated terraces.

As regards ARPES, in the last decade or so the most important work on oxides has focused on the electronic structure of high-T_c cuprate superconductors and related materials. One example of this activity, utilizing synchrotron radiation as an excitation source, is a very recent study by Kaminski *et al* of the Fermi edge region of $Bi_2Sr_2CaCu_2O_{8+\delta}$ (Bi2212) [13]. Working at the SRC, Wisconsin, they have acquired photoemission data, both above and below T_c, with extremely high energy and momentum resolution, from a region of momentum space (k-space) where the states are highly dispersive and where, below T_c, the superconducting gap vanishes (nodal point). Their aim was to determine the intrinsic line shape at this location in k-space, and so determine if and when quasiparticles [14] exist. These measurements are significant as they aid in the understanding of various properties of cuprate superconductors, including charge transport. Figure 4(a) demonstrates the technical excellence of their data, in

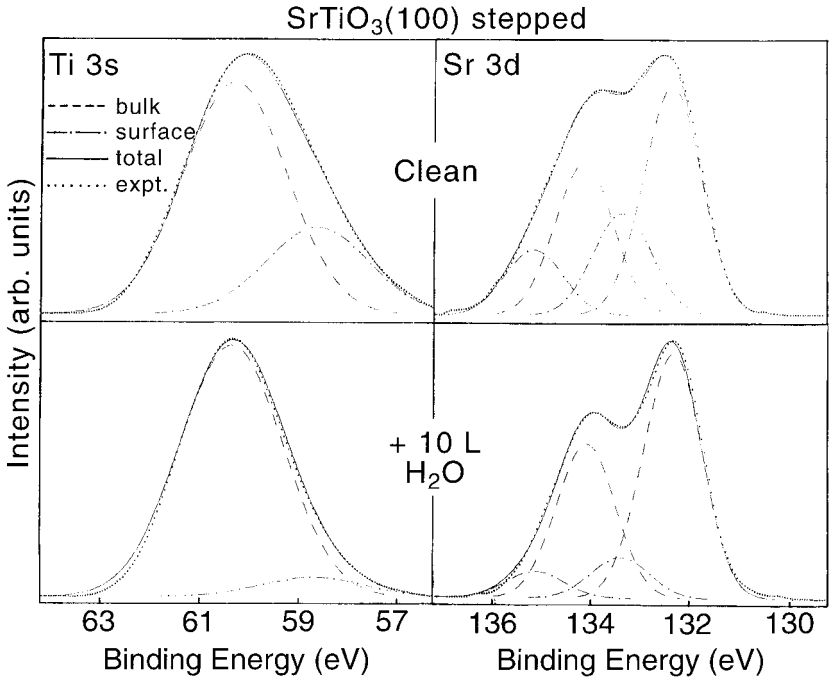

Figure 3. Ti 3s and Sr 3d photoemission spectra of clean and H_2O-dosed stepped $SrTiO_3(100)$, recorded at $h\nu = 110$ eV (Ti 3s) and $h\nu = 180$ eV (Sr 3d). The spectra have been background subtracted and fitted to symmetric Gaussian peaks. Binding energy is referenced to the valence band maximum. Both the bulk and surface Sr 3d features are spin–orbit split by ≈1.8 eV. (After reference [11].)

terms of resolution. In this diagram, two spectra (broken and solid lines), both recorded below T_c at point N in the Brillouin zone (see the inset), are compared. The broken-line spectrum is representative of the resolution obtained previously, and the solid line is that obtained in the currently described work. The improvement, which is demonstrably apparent, has enabled Kaminski *et al* to directly show that quasiparticles exist at this point in k-space. Evidence for quasiparticle states is derived from both the sharpness of the intense peak in the spectrum, and the presence of a clear break in the spectrum between the coherent quasiparticle part of the spectral function and the incoherent part, as indicated by the arrow. Above the superconducting transition temperature they found that there were no quasiparticles. This loss is evidenced by the change in line shape in figure 4(b), which displays spectra acquired at point N as a function of temperature. At temperatures corresponding to the normal state, the trailing edge of the spectral peak gradually evolves into an incoherent tail, rather than there being a clear break.

2.2. Resonance photoelectron spectroscopy (ResPES)

Photoemission from valence band states is modified near core-level thresholds, where the independent-electron approximation breaks down. This so-called resonance photoemission [15] is of particular interest for understanding the valence electronic structure of transition metal and lanthanide oxides. It occurs when a transition from a ground state to a final state can proceed via two or more channels, which then interfere. For example, at the transition metal $M_{2,3}$ x-ray absorption edge of a first-row transition metal compound, there is interference

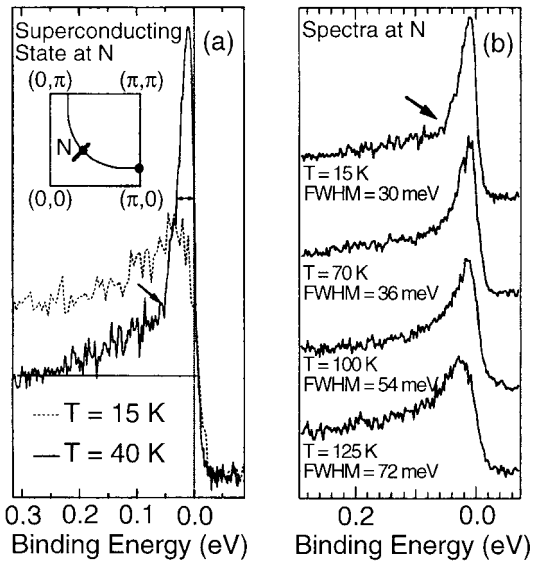

Figure 4. ARPES spectra of Bi2212 recorded (a) below T_c (89 K) at point N (see the inset) for two values of the resolution: FWHM = 105 meV (broken line), FWHM = 30 meV (solid line), (b) as a function of temperature at point N [13]. The arrow indicates a clear break in the line shape (see the text for details).

between the direct photoemission channel:

$$(3p^6 3d^n) + h\nu \rightarrow (3p^6 3d^{n-1}) + e$$

and a resonant channel involving 3p photoexcitation followed by super-Coster–Koster–Kronig decay:

$$(3p^6 3d^n) + h\nu \rightarrow (3p^5 3d^{n+1})^*$$
$$(3p^5 3d^{n+1})^* \rightarrow (3p^6 3d^{n-1}) + e.$$

Experimentally, this interference is observed as an increase (decrease) (resonance (anti-resonance)) in the intensity of the 3d photoemission features as the photons are tuned through this energy region. Such measurements are useful for identifying the origin of features in the valence region, including band-gap states.

Prabhakaran *et al* employed ResPES to investigate charge transfer across the alkali metal/metal oxide interface formed by depositing 0.25 ML of K onto a defect-free (100) surface of rutile TiO_2 [16]. Adsorption of K creates band-gap states which lie at a similar binding energy, about 1 eV, to states created by O vacancies. In the latter case, the states are known to be Ti $3d^1$ in character, due to the reduction of surface Ti^{4+} cations, nominally to Ti^{3+}. ResPES data (figure 5), recorded at the Ti $L_{2,3}$ edge, from the $TiO_2(100)$/K interface show a clear resonance, indicating that the K-induced band-gap states also have Ti 3d character. Also shown in figure 5 are the resonance behaviours exhibited by O-vacancy-induced band-gap states of $SrTiO_3(001)$ and the Ti 3d band of $Ti_2O_3(10\bar{1}2)$. The similarity of these spectra to that for $TiO_2(100)$/K further evidences the Ti 3d character of the band-gap states formed upon K adsorption.

Single-crystal, (100)-oriented CuO has also been the subject of ResPES measurements [17]. These data were collected at the SRS, Daresbury, from a sample cleaved *in situ*. The aim of this study was to probe the character of various parts of the valence band region, and to compare the experimental results with configuration interaction calculations [18]. In figure 6(a)

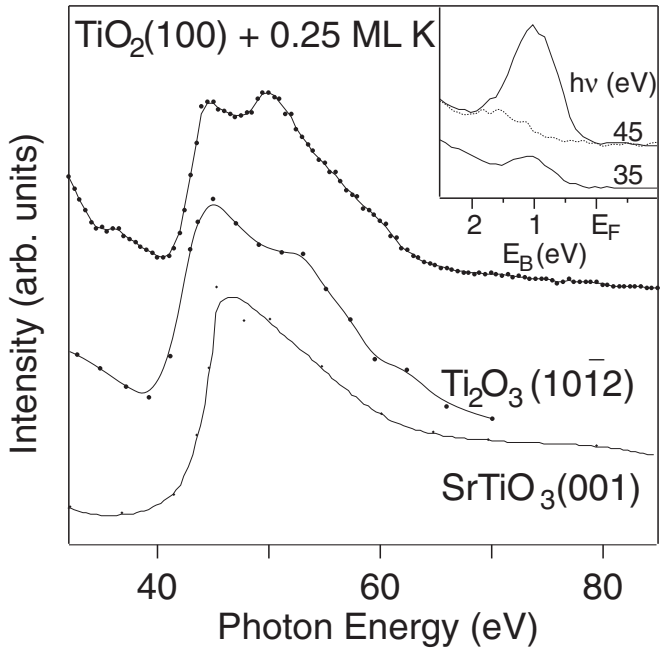

Figure 5. Constant-initial-state (CIS) photoemission spectra of band-gap-state intensity through the Ti 3p resonance for $TiO_2(100) + 0.25$ ML K compared with that for O-vacancy-induced band-gap states on $SrTiO_3(001)$ and the 3d band of $Ti_2O_3(10\bar{1}2)$. The inset shows band-gap-state photoemission spectra from $TiO_2(100) + 0.25$ ML K; the dotted curve shows the same region of the $TiO_2(100)1 \times 1$, $h\nu = 45$ eV spectrum. Spectra were recorded at 300 K, normal emission and a 45° angle of incidence. (After reference [16].)

a valence band photoemission spectrum of CuO(100) from reference [17] is displayed. The main weight of the valence band is located at binding energies between approximately 1 eV and 8 eV, with smaller features at higher binding energies. ResPES data at the Cu 3p → Cu 3d threshold were collected from various locations in the valence region, as indicated in figure 6(a). These data are displayed in figure 6(b). From the observation that only the higher-binding-energy satellite features show significant resonance, the authors concluded that the main part of the valence band arises principally from $d^9\underline{L}$ final states, whereas the satellite features are due to d^8 final states (the $d^9\underline{L}$ final state cannot be accessed directly via intra-atomic Auger decay from the excited state created at resonance). This interpretation is consistent with the CI calculations [18].

2.3. Photon-stimulated ion desorption (PSID)

There was much interest in PSID in the 1970s and 1980s as a means to explore bonding of atoms and molecules to surfaces [19]. Maximal valency oxide substrates were a particular focus of attention, because they represented prototype systems with which to test what is termed the Knotek–Feibelman (KF) model of positive-ion desorption. The basic principle of this model involves ionization of a core level of a surface anion or cation bonded to the anion leading, via intra-atomic or inter-atomic Auger decay, respectively, to a *Coulomb explosion*, resulting in the positive ion of the surface anion being repelled into the vacuum. Maximal valency prevents decay of the core hole from filled cation valence states.

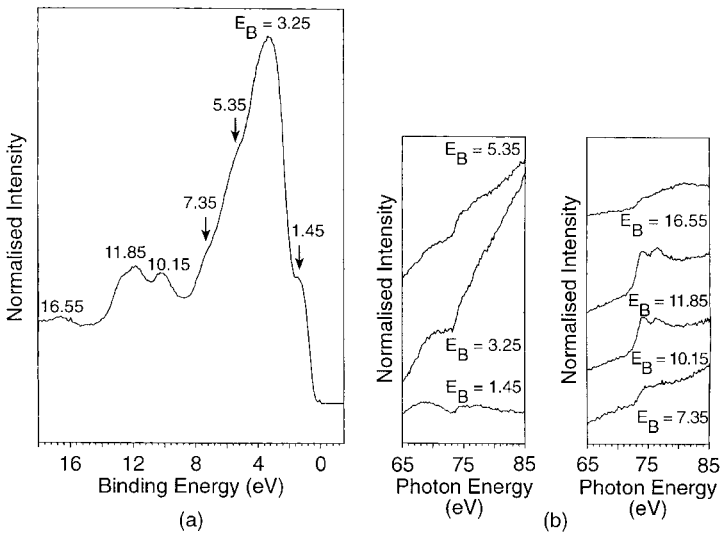

Figure 6. (a) The PES valence band spectrum of CuO(100), marked with the binding energy positions selected for ResPES (CIS) measurements. (b) ResPES data acquired at the Cu 3p → Cu 3d threshold for the various binding energies (eV) indicated in (a) [17].

Analogous models to the above can be constructed for adsorbates, on which basis bond sites can be identified. For instance, if H is bonded to O at the surface of an oxide, then ionization of an O core level is expected to result in H^+ desorption, whereas if H is bonded to a cation, then ionization of a cation core level will give rise to desorption. In addition, it should be possible to use the ion yield to probe the environment of an atom to which the ion was bound by way of the surface extended x-ray absorption fine structure (SEXAFS). It seems, however, that mechanisms other than KF can dominate, in particular x-ray-induced electron-stimulated desorption (XESD), where energy is carried from near-surface photon absorption to the surface by way of secondary electrons, and the Menzel–Gomer–Redhead mechanism [19]. These make it very difficult to employ the ion yield as a probe of the surface structure.

As an example of the application of PSID to oxide surfaces we present results obtained from the stepped –OH-covered $SrTiO_3(100)$ surface described above [10]. The goal of this experiment was to explore the mechanism for ion desorption. Ion-yield data were acquired with a time-of-flight (TOF) mass spectrometer at the SRS, Daresbury, operating in single-bunch mode. Figure 7 shows the variation in the H^+ and OH^+ yields above the Ti K edge (4966 eV), along with corresponding total-electron-yield (TEY) and fluorescence-yield spectra. A dominating XESD contribution to the ion-yield spectra is evidenced by the similarity of the TEY, fluorescence-yield and ion-yield spectra. This suggests that the three types of spectrum arise from ionization of titanium atoms having the same local environment. Since the TEY and fluorescence spectra are dominated by a bulk atom contribution, this indicates the dominance of a secondary, non-local mechanism of PSID.

2.4. Surface extended x-ray absorption fine structure (SEXAFS)

SEXAFS [20, 21], the surface analogue of EXAFS, was developed in the mid- to late-1970s. This technique provides information about the local geometric environment of absorbing atoms, including bond distances and coordination numbers. Synchrotron radiation is essential

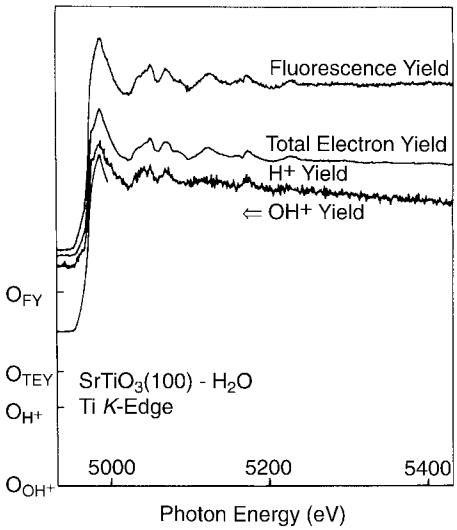

Figure 7. The H^+ and OH^+ photon-stimulated ion desorption yields from stepped $SrTiO_3(100)$ following exposure at 300 K to H_2O. The total electron and fluorescence yields are shown for comparison. (After reference [10].)

for SEXAFS, as an intense source of continuously tunable photons is required. The linear polarization of the x-rays is also generally utilized to aid structure determination. SEXAFS has been applied most often to the elucidation of the local structure of adsorbed species. Amongst these studies are a number concerning adsorbates on metal oxide substrates.

An early SEXAFS study of a metal oxide surface investigated the local geometry of K in $TiO_2(100)c(2 \times 2)K$ [16]. Data were acquired at the potassium K edge in two measurement geometries, i.e. normal and grazing x-ray beam incidence with the electric vector aligned with the [001] azimuth (see figure 8). Successful modelling of the SEXAFS oscillations, using appropriate electron scattering code, required a single shell of oxygen neighbours at 2.62 ± 0.03 Å, the analysis rejecting models which contained K or Ti backscatterers. Adsorption site determination entailed a comparison of the experimentally determined oxygen effective coordination numbers with those calculated for four plausible sites: angled bridge, atop bridge, atop and K inclined (figure 8). From this process it was concluded that the angled bridge is the K adsorption site, in which the K–O_2 plane is at 45° to the surface normal. It is noted

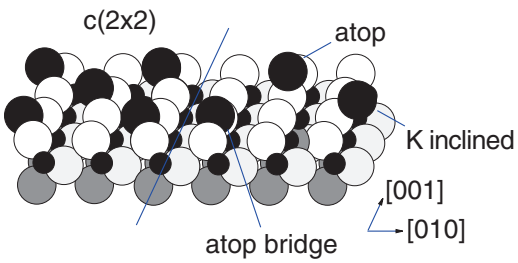

Figure 8. A schematic diagram of the $TiO_2(100)c(2 \times 2)K$ surface derived from SEXAFS data [16], with K atoms bonded to two bridging oxygens (left). The alternative K adsorption sites are also shown (right).

in the paper that the K–O bond length is close to the sum of the appropriate ionic radii. The structure predicted by a recent *ab initio* Hartree–Fock calculation is in excellent agreement with the experimental data [22].

SEXAFS has also been utilized to probe the structure of nanoscale metal films/clusters deposited on metal oxide substrates. An example of such work is that by Gota *et al* who have examined α-$Al_2O_3(0001)1 \times 1$–Cu and α-$Al_2O_3(0001)(\sqrt{31} \times \sqrt{31})R\pm9^\circ$–Cu with Cu K-edge SEXAFS, following deposition of 0.5 ML equivalent of Cu [23]. For this study SEXAFS spectra were obtained at normal photon incidence. On both surfaces it was found that the majority of Cu is present in the form of nanoclusters, with those formed on the (1×1) surface being slightly smaller than those on the reconstructed surface. Information about the interface was also extracted. Specifically, including a shell of Al scatterers was found to significantly improve the fit between theory and experiment. It should be noted that no evidence for oxygen scatterers was found. Table 1 lists the structural parameters obtained from analysis of the SEXAFS. The authors interpret the rather long Cu–Al bond distances as possibly being a consequence of the very weak interaction between Cu and the Al_2O_3 surfaces The relatively high effective coordination number of Al for the $(\sqrt{31} \times \sqrt{31})R\pm9^\circ$ reconstruction (5.7) is ascribed to Cu adsorption at defects.

Table 1. Results of best fits to SEXAFS modulations, recorded at normal incidence, from $Al_2O_3(0001)1 \times 1$–Cu and $Al_2O_3(0001)(\sqrt{31} \times \sqrt{31})R\pm9^\circ$–Cu at 0.5 ML equivalent coverage of Cu [23]. N^* is the effective coordination number of a shell of scatterers, R is its distance and $\Delta\sigma^2$ the mean square relative displacement.

	N^* ($\pm10\%$)	R (Å) (±0.02 Å)	$\Delta\sigma^2$ (Å^2) ($\pm0.5 \times 10^{-3}$)
(1×1)			
Cu–Cu	0.7	2.0	0.010
Cu–Cu	4.3	2.37	0.010
Cu–Al	2.0	3.16	0.010
$(\sqrt{31} \times \sqrt{31})R\pm9^\circ$			
Cu–Cu	4.7	2.42	0.012
Cu–Al	5.7	3.24	0.012

One other study that should be mentioned in this section is a determination of the adsorption geometry of molybdenum oxides on $TiO_2(110)$ in the submonolayer regime [24, 25]. Unusually, in terms of the work described in this review, data were accumulated under atmospheric conditions rather than in a UHV chamber. Also the measurements were not performed using the typical SEXAFS methodology, but rather employed polarization-dependent total-reflection fluorescence (PTRF) EXAFS. Briefly, this approach involves collecting fluorescence-yield data for different orientations of the surface relative to the x-ray electric vector with the photon incidence angle always maintained below the critical angle for total reflection. For the $TiO_2(110)$ surface the measurement geometries were $\boldsymbol{E} \parallel [110]$, $\boldsymbol{E} \parallel [001]$, and $\boldsymbol{E} \parallel [1\bar{1}0]$. The overlayer was formed by impregnating a sample, which had been annealed at 823 K for two hours in air to remove surface impurities, with an ultrapure aqueous solution of $(NH_4)_6Mo_7O_{24}{\cdot}4H_2O$, followed by oxidation at 773 K for three hours. The Mo coverage after this procedure was approximately 0.2 ML. Data analysis was carried out by comparing theoretically simulated spectra generated for many different trial structures with the experimental data. The best fit between experiment and theory was obtained for a Mo edge-shared dimer structure. Both the internal structure of the Mo dimer and the dimer–substrate

bonding were determined. It was found that the Mo–Mo dimer axis lies parallel to the [1$\bar{1}$0] direction of TiO_2(110), that the Mo dimer is centred on the bridging row oxygens such that the two Mo atoms bond to two bridging oxygens and that these bridging oxygens are significantly shifted from their clean-surface positions. A schematic diagram of the optimized structure is displayed in figure 9, and the values of the corresponding inter-atomic distances are listed in table 2.

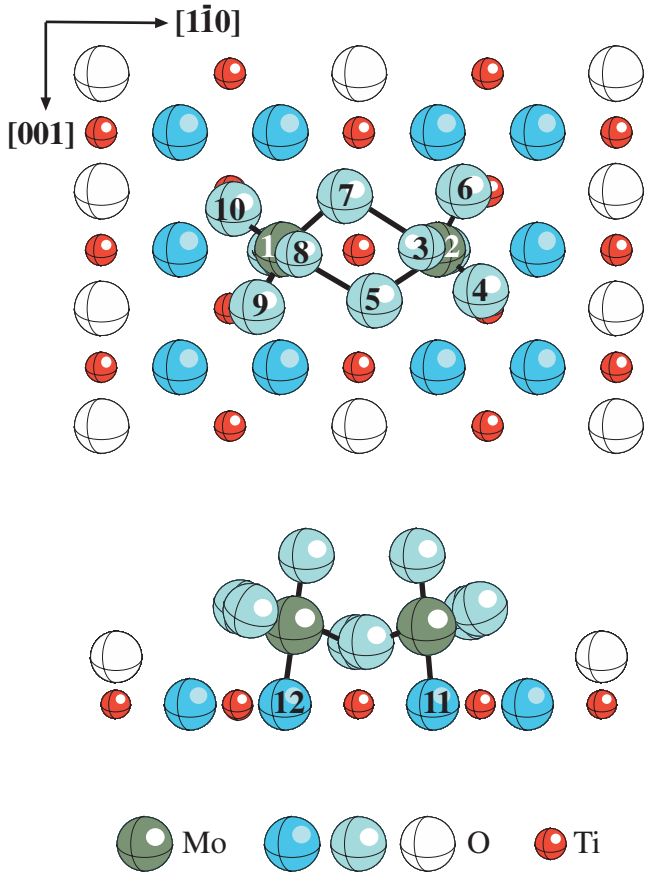

Figure 9. Plan and side views of the structure of molybdenum oxide dimers on TiO_2(110)1 × 1 [24, 25]. The numerical labels are employed in table 2.

2.5. Near-edge x-ray absorption fine structure (NEXAFS)

Elucidation of molecular adsorbate orientation is the principal use of NEXAFS [26] in the surface science community. One of the attractions of this technique lies in the relative ease of data analysis, relying only on a knowledge of an adsorbate's molecular orbitals, substrate symmetry and the application of trigonometric functions. This simplicity enables one to utilize NEXAFS for obtaining structural information from rather complex adsorption systems, which may be intractable with other surface structure techniques, e.g. large adsorbate molecules, complex surfaces and defect adsorption. As NEXAFS spectra are sensitive to local electronic structure, in addition to the determination of molecular orientation, they can also be used to

Table 2. Bond lengths for optimized Mo dimer structure on $TiO_2(110)1 \times 1$ [24, 25]. The numerical labelling of the atoms corresponds to that in figure 9.

Atoms	Bond length (Å)
Mo1–Mo2	3.35 ± 0.08
Mo1–O5	2.32 ± 0.08
Mo1–O7	1.92 ± 0.08
Mo1–O8	1.79 ± 0.05
Mo1–O9	1.78 ± 0.08
Mo1–O10	1.69 ± 0.08
Mo1–O12	2.20 ± 0.09
Mo2–O3	1.79 ± 0.05
Mo2–O4	1.69 ± 0.08
Mo2–O5	1.92 ± 0.08
Mo2–O6	1.78 ± 0.08
Mo2–O7	2.32 ± 0.08
Mo2–O11	2.20 ± 0.09

fingerprint chemical species, and so identify, for example, surface reaction products. Both of these applications of NEXAFS have been used to advantage in work on metal oxide surfaces.

Single-crystal zinc oxide surfaces have been the focus of significant effort, as regards the determination of adsorbate angular orientation using NEXAFS [27, 28]. An example of this work is a C and N K-edge study of the aromatic molecule pyridine (C_5H_5N) on $ZnO(10\bar{1}0)$ [29]. The pyridine adlayer, of coverage approximately 0.1 ML, was formed on the ZnO surface by exposure to 1 L at the measurement temperature of 295 K. NEXAFS data were recorded at a series of polar photon incidence angles, with the electric vector of the linearly polarized photons either parallel or perpendicular to the surface Zn–O dimer rows. The NEXAFS spectra show that pyridine stands up on the surface with the ring plane in the $[000\bar{1}]$ azimuth. Two C K-edge spectra, recorded at normal and grazing incidence with the electric vector in the $[11\bar{2}0]$ azimuth, are displayed in figure 10. The inset in this figure shows the intensity variation of the strongest π^*-feature (a doublet, with components at 285.0 eV and 285.5 eV) with angle of photon incidence in the two measurement azimuths, along with the best fits to these data using an appropriate trigonometric expression [26]. These fits correspond to a tilt of the molecular plane towards the surface of 28° and a 27° twist out of the $[11\bar{2}0]$ azimuth. Analysis of the N K-edge data produced a consistent result. An adsorption geometry compatible with the NEXAFS data is shown in figure 11. The authors note that the apparent distortion out of a high-symmetry geometry should be viewed with some caution, since dynamical effects are known to significantly influence NEXAFS results obtained at room temperature.

N K-edge NEXAFS has also been employed by Patthey *et al* to investigate the adsorption of bi-isonicotinic acid (2, 2′-bipyridine-4, 4′-dicarboxylic acid), a ligand present in a number of photochemically important organometallic dyes, on $TiO_2(110)1 \times 1$ [30]. Measurements, as a function of photon incidence angle, were recorded from two $TiO_2(110)$ samples mounted such that one had the electric vector of the x-ray beam parallel to the bridging oxygen rows (see figure 12) whilst for the other it was perpendicular. A submonolayer coverage of adsorbate was obtained by deposition at a substrate temperature of 473 K. O 1s photoemission data were interpreted as indicating that for such a submonolayer coverage the two –COOH groups are deprotonated and that all four oxygens are equivalent. From the angular dependence of the leading N K-edge π^*-resonance it was determined that the molecules are oriented with a tilt angle of 25° with respect to the surface normal and twisted 44° out of the [001] azimuth. It is, however, not possible from these data to distinguish between an adsorption geometry with the

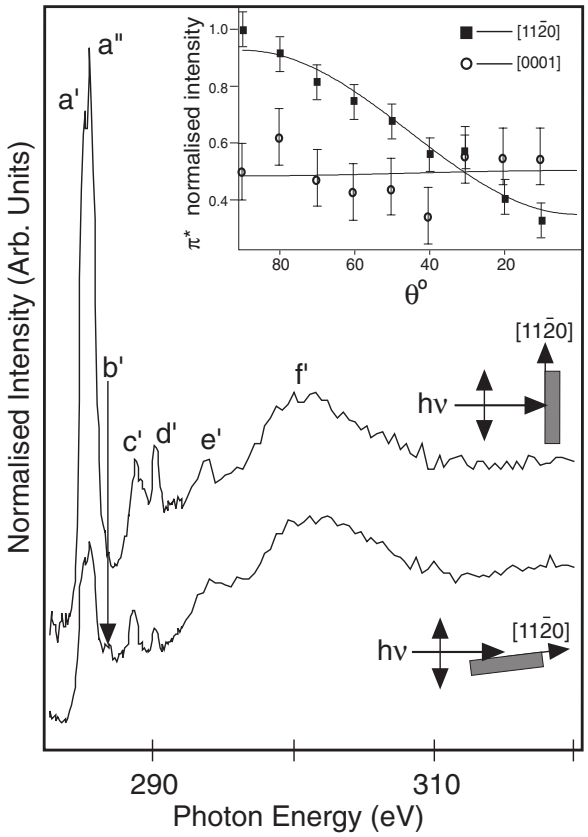

Figure 10. C K-edge NEXAFS spectra of ZnO(10$\bar{1}$0) after exposure to 1 L of pyridine at the measurement temperature of 295 K [29]. The peak labels are discussed in reference [29]. The inset shows the variation in intensity of the π^*-feature (peaks a′ and a″) with angle of incidence in the two measurement azimuths (data points). This is compared with the best fit to the data (solid lines).

two rings of the molecule coplanar, and one in which they are twisted relative to one another. Complementary periodic INDO calculations were performed for several possible adsorption geometries. Figure 12 shows the lowest-total-energy adsorption structure, which agrees well with the NEXAFS analysis.

The final study to be discussed in this section is concerned with examining the thermally activated reaction of SO_2 with $TiO_2(100)1 \times 1$ and $TiO_2(100)1 \times 3$, employing S K-edge NEXAFS measurements [31]. In this case the spectra were used both to determine adsorbate orientation, and to identify the chemical nature of the adsorbed species by comparison with spectra acquired from model compounds (i.e. TiS_2, Na_2SO_3, Na_2SO_4 and $CuSO_4$). It was concluded that the interaction of SO_2 with the 1×1 and 1×3 terminations is very similar. At 110 K, SO_2 is chemisorbed, and forms a sulphite-like (SO_3^{2-}) species at higher temperatures (110–400 K). SO_3^{2-} reacts further to produce a sulphate-like (SO_4^{2-}) surface species (130–500 K). To investigate the orientations of these three surface moieties, NEXAFS spectra were recorded over a range of polar photon incidence angles with the x-ray electric vector in the [001] and [010] sample azimuths. These measurements were performed at three substrate temperatures, namely 130 K, 200 K and 500 K, in order to focus on SO_2, SO_3^{2-} and SO_4^{2-},

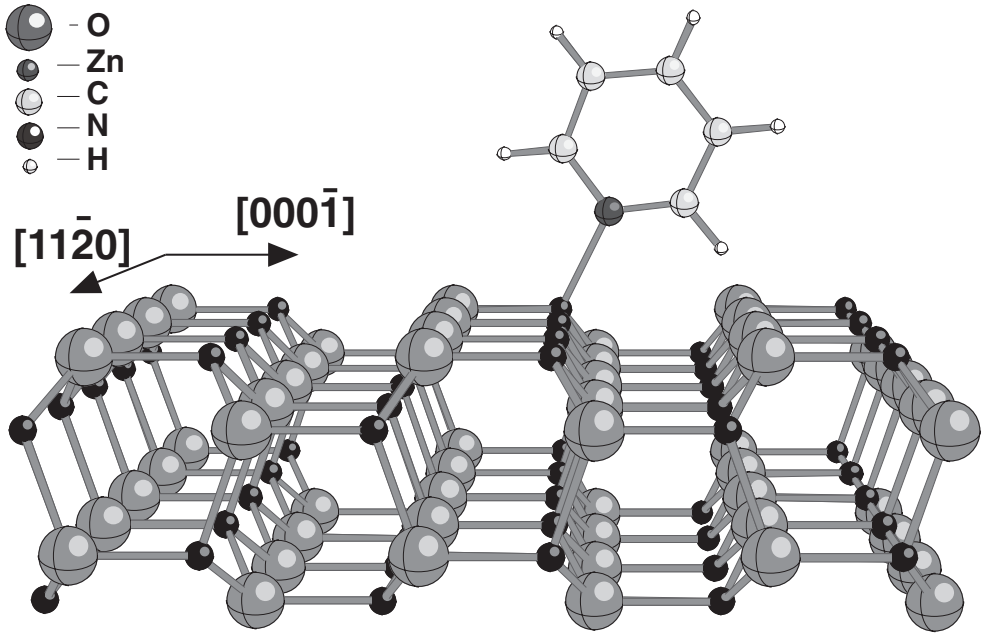

Figure 11. A model of a bulk-terminated ZnO(10$\bar{1}$0) surface, with an adsorbed pyridine molecule oriented such that it is consistent with NEXAFS results [29].

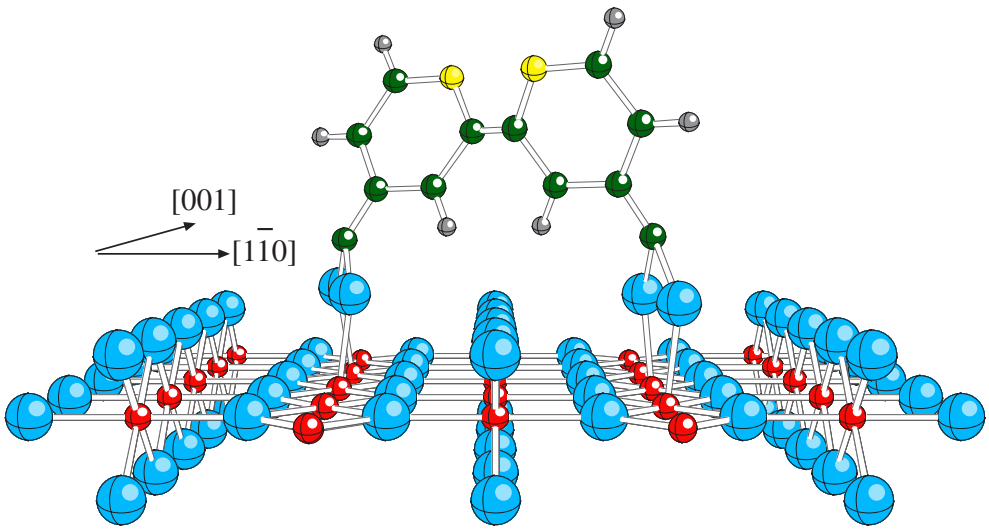

Figure 12. A schematic diagram of the theoretically calculated lowest-energy adsorption structure for bi-isonicotinate on TiO_2(110)1 × 1. This geometry is consistent with NEXAFS data [30]. In the adsorbate, the light spheres in the rings are N, the dark spheres are C, the smallest spheres are H and the largest spheres are O atoms.

respectively. For SO_2, analysis of the π^*-resonance indicates that the C_2 molecular axis is oriented $20^\circ \pm 2^\circ$ away from the (100) surface normal on the (1×3) surface, and $26^\circ \pm 3^\circ$ on

the (1 × 1) surface, with no azimuthal alignment on either surface. It should be noted that at 110 K SO_2 displayed no specific orientation on either surface.

A similar analysis for SO_3^{2-}, which adopts a trigonal-based pyramidal structure, again indicates no azimuthal alignment. Tilts of the C_3 molecular axis of 24° ± 3° and 25° ± 3° away from the surface normal are observed on the (1 × 3) and (1 × 1) surfaces, respectively. Data for SO_4^{2-} from both surfaces at 500 K show little photon incidence angle dependence. This is consistent with a sulphate species having T_d symmetry, although there is evidence from the spectral features of some distortion away from this highly symmetric configuration. This distortion is more pronounced for the SO_4^{2-} already present on the surfaces at lower temperatures, specifically between 130 K and 220 K. As the results from the (1 × 1) and (1 × 3) surfaces are so similar, the authors use these structural data to argue that the reaction of SO_2 with TiO_2 is driven by local geometry effects rather than longer-range surface structure. Proposed adsorption structures for the various surface species on the two surfaces are shown in figure 13.

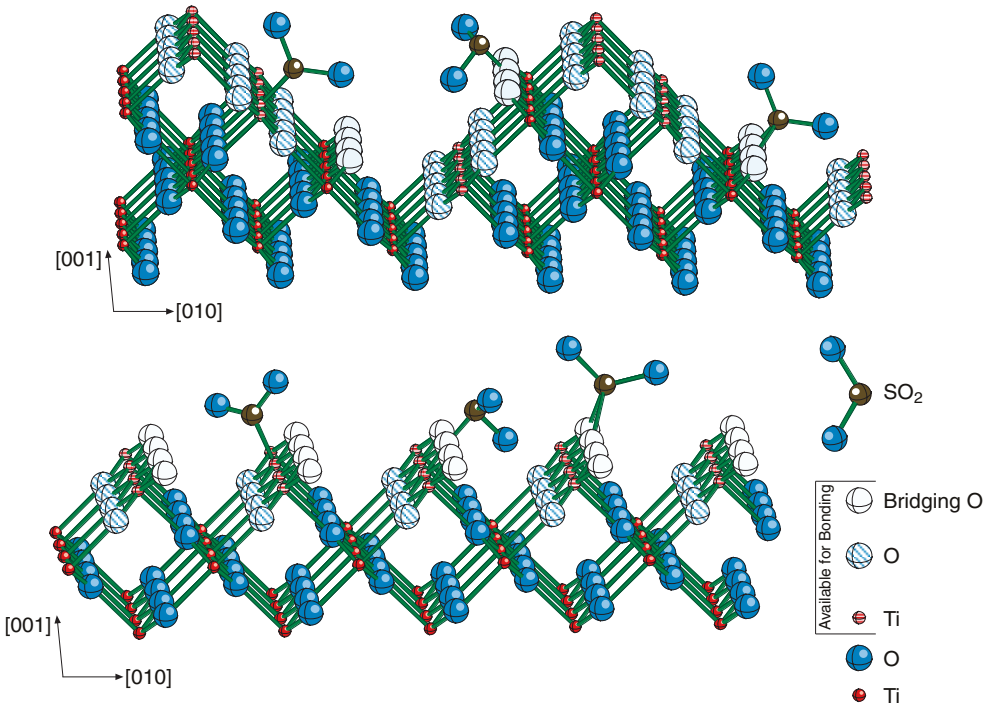

Figure 13. Models of $TiO_2(100)1 \times 3$ (top) and $TiO_2(100)1 \times 1$ (bottom) along with the proposed SO_2 adsorption sites corresponding to, from left to right, chemisorbed SO_2, SO_3^{2-} and SO_4^{2-}-like species [31].

2.6. X-ray standing waves/normal-incidence x-ray standing waves (XSW/NIXSW)

XSW and NIXSW are well-established quantitative structural techniques [32, 33]. The fundamental basis of these techniques is that as one scans, in either angle (XSW) or energy (NIXSW), through the finite width of a Bragg reflection in a periodic lattice, a standing wavefield, created by coherent coupling between the incident and diffracted photon beams,

moves continuously, changing its position by a total of one half of a diffraction plane spacing. Thus it is possible to obtain an estimate of the perpendicular separation between an atom and a diffraction plane by measuring the x-ray absorption of the atom as a function of the position of the wavefield. As indicated above, an XSW experiment is performed by scanning in angle through the Bragg condition, whereas the NIXSW technique, which was developed latterly by Woodruff *et al* [33], involves energy scanning. In addition, for NIXSW measurements the Bragg condition is fulfilled with the x-ray beam normal to the diffraction planes.

NIXSW studies on both clean and adsorbate-covered metal oxides have been carried out by researchers at SSRL, Stanford. For example, they have undertaken NIXSW measurements on the (100) surface of a UHV-cleaved CaO single crystal, which exhibited a (1 × 1) LEED pattern [34]. In this experiment, data were acquired by monitoring Ca LMM and O KLL Auger electrons as the photon energy was swept through the (200) Bragg condition. These data allowed relaxations perpendicular to the surface plane, including rumpling, to be determined. It was found that, within experimental error, the surface atoms were not shifted away from their bulk-terminated positions.

As for an adsorbate system, the Stanford group have investigated water adsorption on MgO(100) [35]. They recorded NIXSW data from cleaved MgO(100) samples following two different overlayer preparations: (i) exposure to a partial pressure of 1×10^{-3} Torr of water for 3 min at 300 K and (ii) immersion in water at 300 K for 10 min. Only (1 × 1) LEED patterns were observed after either preparation, although the intensity variation of the diffraction spots from the sample immersed in water were apparently somewhat different, possibly suggesting a modified surface structure. From previous photoemission data [36], recorded by the same group from similarly prepared surfaces, it was concluded that the adsorbed moiety resulting from both preparations is surface hydroxyl, present at coverages of 1.2 ML and 2 ML for preparations (i) and (ii), respectively (the coverages greater than 1 ML arise simply due to fact that besides the binding of OH^- species, formed following H_2O dissociation, to surface Mg^{2+} sites, the H^+ counter-ions also form hydroxyl species by attachment to oxygen anions in the surface layer (see figure 14). NIXSW data were obtained from the MgO(200) diffraction planes, thus providing information about the position of atoms along the surface normal. The locations of both oxygen and magnesium atoms were elucidated using the O KLL and Mg KLL Auger signals, respectively. For both preparations it was concluded that the perpendicular separation between the oxygen atom of the hydroxyl and the surface layer is 2.13 ± 0.04 Å. Assuming, as the Stanford group have done, that the hydroxyls are bonded to the surface Mg cations so that the Mg–O bond lies along the surface normal, then this distance of 2.13 ± 0.04 Å represents the Mg–OH bond length (figure 14). Additionally, they found that surface hydroxylation does not induce any vertical shift in the top-layer Mg cations. Somewhat surprisingly, at least initially,

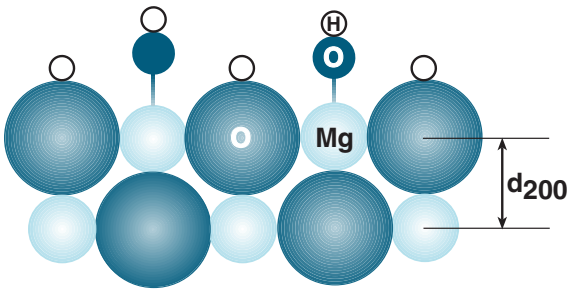

Figure 14. A cross-section of the fully hydroxylated MgO(100) surface proposed in reference [35].

the derived Mg–OH distance is equal, within experimental uncertainty, to the Mg–O bond length in the bulk oxide (2.106 Å). The authors note, however, that the Mg–O bond lengths in bulk MgO and $Mg(OH)_2$ have been shown to be the same from diffraction studies [37].

2.7. Surface x-ray diffraction (SXRD)

First performed in the late 1970s, the surface structure technique SXRD has been shown to be capable of determining atomic positions to a high degree of accuracy [38]. The surface sensitivity of these photon in/photon out measurements is derived from the very grazing angles of x-ray incidence employed, ideally below the critical angle for total external reflection, which limit the penetration depth of the x-rays. Synchrotron radiation is necessary for SXRD as scattered light intensity is low, and so a high photon flux is required to obtain sufficient statistics on a reasonable timescale. Usually, the experiment involves collecting data (rocking scans) both for a small value of l at different (h, k) in reciprocal space (*in-plane* data), and over a range of l at fixed (h, k) (crystal truncation rod (CTR) scans). The results of these measurements can be used to determine displacements of atoms both laterally and vertically. Concerning the data analysis, SXRD has the advantage, over electron diffraction techniques, that x-rays only interact weakly with matter, and so kinematic theory is valid.

A number of groups are now utilizing SXRD to study metal oxide surfaces (see references [39] and [40] for two detailed reviews). Amongst the studies they have performed is the first quantitative structural determination of the prototypical metal oxide surface $TiO_2(110)1 \times 1$ [41]. In this study SXRD data were collected at both the SRS, Daresbury, and the ESRF, Grenoble. In total five CTRs were measured, including the specular rod at $(h, k) = (0, 0)$. The degree of relaxation of the (1×1) surface away from bulk termination was determined by fitting these experimental CTRs to theoretically simulated data. Thirteen structural parameters were optimized in the refinement. Figure 15 shows the atomic displacements found from this procedure. The largest relaxation is that of the bridging oxygen (O(1) in figure 15) which moves into the surface by 0.27 ± 0.08 Å. The sixfold-coordinated Ti (Ti(1)) relaxes 0.12 ± 0.05 Å

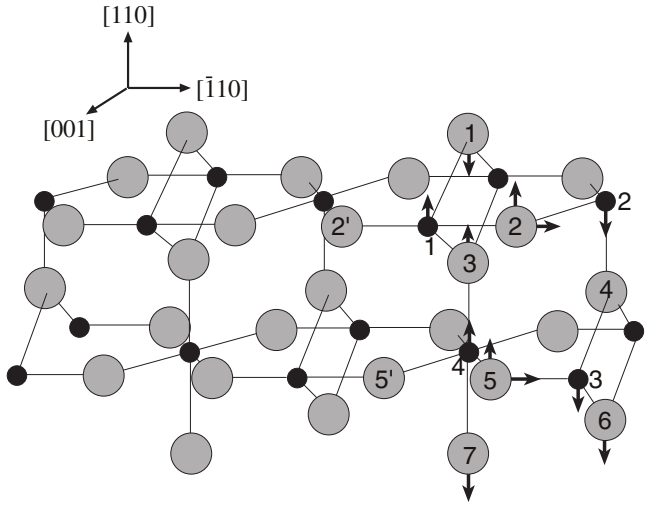

Figure 15. A real-space model of bulk-terminated $TiO_2(110)1 \times 1$ from reference [41]. Small black circles represent Ti and large grey circles O. The arrows indicate the direction of the relaxations determined by SXRD. The atom types varied in the structural refinement are shown.

outwards, whilst fivefold-coordinated Ti atoms (Ti(2)) move into the surface by 0.16 Å, causing a rumpling of the surface Ti layer. In terms of the Ti positions, there is good agreement between the SXRD results and a theoretical calculation by Ramamoorthy *et al* [42].

One other example of an SXRD study is that performed by Renaud's group on the surface structure formed following the segregation of Ca to the surface of MgO(100) [43]. For this work the segregation was induced by annealing a sample at 1773–1873 K in air for several hours—the first step in a procedure developed for preparing high-quality (100) surfaces of MgO. To remove both carbon contamination and oxygen vacancies, the MgO(100)–Ca surface was further annealed at approximately 1173 K for 30 min in 1×10^{-4} Torr of O_2 in the UHV measurement chamber. Surface coverage of Ca was estimated to be of the order of 1 ML from Auger electron spectroscopy, and a $(\sqrt{2} \times \sqrt{2})$R45° surface unit cell was observed. The structure was elucidated by fitting the $(11l)$ and $(20l)$ crystal truncation rods. For the optimization it was assumed that (i) Ca is at substitutional sites and (ii) Ca is present only in the topmost atomic plane. The best fit to the experimental data was obtained for a structure having the observed $(\sqrt{2} \times \sqrt{2})$R45° surface unit cell, in which every other surface Mg cation is replaced by a Ca cation. A schematic diagram of the structure is displayed in figure 16, and the vertical displacements of the atoms in the first two layers are listed in table 3. Qualitatively similar atomic positions were obtained from theoretical calculations performed on the $(\sqrt{2} \times \sqrt{2})$R45° unit cell, which was found to be energetically favourable [44–47].

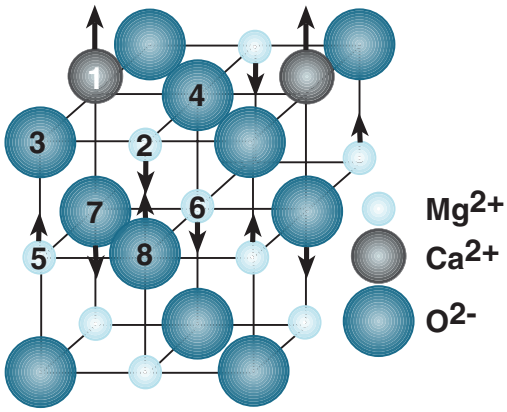

Figure 16. The optimum structure of the Ca-segregated MgO(100) surface determined from SXRD [43]. The numerical labels are employed in table 3.

Table 3. z-displacements of atoms in MgO(100)$(\sqrt{2} \times \sqrt{2})$R45°–Ca from analysis of SXRD data [43]. The numerical labelling of the atoms corresponds to that in figure 5. Both absolute displacements (Δz (Å)) and shifts relative to the MgO bulk nearest-neighbour distance ($\Delta z/d$) are listed.

	1: Ca	2: Mg	3: O	4: O	5: Mg	6: Mg	7: O	8: O
$\Delta z/d$	0.3	−0.032	0 (fixed)	0 (fixed)	0.095	−0.2	−0.2	0.2
	±0.10	±0.066	±4	±4	±0.014	±0.08	±0.14	±0.06
Δz (Å)	0.63	−0.066	0	0	0.20	−0.42	−0.42	0.42
	±0.03	±0.14	±9	±9	±0.03	±0.18	±0.32	±0.12

2.8. Photoelectron diffraction (PhD)

PhD [48, 49] has been developed into a reliable quantitative structural technique over the last ten years, comparable in precision to the traditional surface structural technique of choice, namely quantitative low-energy electron diffraction (LEED-IV). Primarily utilized as a tool for determining adsorbate structure, a particularly attractive feature of PhD is its elemental and even chemical state specificity. This attribute derives from the fact that the diffraction data are extracted from a particular core-level feature. Such data can be accumulated as a function of core-level kinetic energy (scanned-energy-mode PhD), electron emission angle (scanned-angle-mode PhD) or a combination of the two modes. For scanned-energy-mode PhD, which to date has been utilized most widely for quantitative adsorbate structure determination, synchrotron radiation is a necessary prerequisite due to the need for a continuously tunable source of x-rays. Scanned-angle-mode experiments also benefit hugely from the use of such a photon source.

As regards metal oxide surfaces there are exceedingly few synchrotron radiation studies employing PhD. One work of note is that conducted by Chambers *et al*, who have investigated the structure of the formate moiety ($[HCOO]^-$) on $TiO_2(110)$ using PhD, in both scanned-energy and scanned-angle modes, combined with laboratory-based x-ray photoelectron diffraction (XPD) measurements and *ab initio* total-energy calculations [50–52]. For this study O 1s PhD data were obtained at the Advanced Light Source (ALS), Berkeley, from a $TiO_2(110)1 \times 1$ surface saturated with formate (nominally a coverage of 0.5 ML, where 1 ML corresponds to one formate anion per exposed Ti^{4+}). The chemical specificity of PhD was exploited in this experiment, as two O 1s peaks were apparent, one due to formate and the other due to the substrate, separated by approximately 2 eV. Scanned-angle data were acquired over an azimuthal range of 0–180° for several polar emission angles. On the basis of the theoretical calculations, scanned-energy ($h\nu = 580$–880 eV) data were recorded at 10° away from normal emission in the [001] azimuth. From analysis of these data, using electron scattering code to simulate the experimental data, it was concluded that formate is bound, via its oxygen atoms, to two neighbouring surface Ti cations in a bridging bidentate conformation, with its molecular plane aligned with the [001] azimuth. The vertical separation between the Ti cations and the formate oxygens was determined to be 2.1 ± 0.1 Å.

More recently, at BESSY, scanned-energy-mode PhD has been employed to determine the adsorption geometry of NO on NiO(100) [53, 54]. To avoid problems associated with sample charging, measurements were performed on a thin film of (100)-oriented NiO grown on Ni(100) rather than single-crystal NiO. PhD spectra were recorded from the N 1s core level. Two peaks, separated by 4.4 eV, were observed. Comparison of the diffraction displayed by each of these peaks demonstrated that the two peaks arise from two different core-hole states of the same surface species. Quantitative elucidation of the geometry of this adsorbate involved a two-step process. Initially, a visual inspection of the PhD spectra was carried out to ascertain the approximate position of the N atom relative to its nearest neighbours below. Next, this geometry was used as an initial guess for the generation of simulated PhD data via electron multiple-scattering calculations, which were compared to the experimental data set. Agreement between experimental and theoretical data was iteratively improved by varying structural parameters until the best fit, and therefore the optimized structure, was obtained. It was concluded that NO adsorbs the N atom down atop a Ni atom, and in agreement with previously published N K-edge NEXAFS data [55], the N–O bond axis is tilted away from the surface normal. The optimized adsorbate geometry is shown in figure 17 and the values of the optimized parameters are listed in table 4. Interestingly, although theoretical calculations (e.g. reference [56]) favour this adsorption geometry, the Ni–N bond length obtained from such work is approximately 0.2 Å longer than the experimentally derived value.

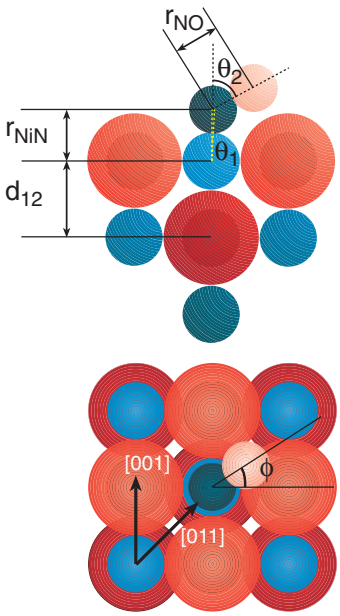

Figure 17. A schematic diagram of the optimum NO adsorption geometry on NiO(100) determined from PhD [53, 54]. The geometrical parameters varied during the structural optimization are displayed. For the adsorbate, the darker shaded circle is nitrogen and the lighter one is oxygen.

Table 4. Parameter values obtained from the best fit between experimental N 1s PhD data and theoretical simulations for NiO(100)–NO [53, 54]. The definitions of the first five parameters are given in figure 17. $\langle u_{\parallel}^2 \rangle$ and $\langle u_{\perp}^2 \rangle$ are the mean square vibrational amplitudes of the nitrogen atom parallel and perpendicular to the surface, respectively. The positive error for r_{NO} is replaced by an asterisk due to the fact that all N–O bond lengths greater than the optimum lie within the estimated error. The double asterisk next to the error for θ_2, the N–O tilt, indicates that the error given is only for N–O bond lengths <1.43 Å.

Parameter	Value
r_{NiN} (Å)	1.88 ± 0.02
θ_1 (deg)	$3 + 3/-8$
r_{NO} (Å)	$1.12 + */-0.15$
θ_2 (deg)	$59 + 31/-17^{**}$
d_{12} (Å)	2.07 ± 0.04
$\langle u_{\parallel}^2 \rangle$ (Å^2)	$(1.8 + 4.2/-1.8) \times 10^{-2}$
$\langle u_{\perp}^2 \rangle$ (Å^2)	$(3.8 \pm 1.9) \times 10^{-3}$

Another PhD study of interest is that performed by Verdini *et al* on the ALOISA beamline at ELETTRA, Trieste. They examined the surface relaxation of clean $TiO_2(110)1 \times 1$ using *variable-polarization* scanned-angle-mode PhD [57]. In this rather novel derivative of the technique, data have to be recorded from an s core level in two different measurement geometries, which differ in the orientation of the electric vector of the linearly polarized x-rays with respect to the surface normal. In one geometry, named transverse magnetic (TM) polarization, $\boldsymbol{E}$ is parallel to the surface normal, whilst in transverse electric (TE) polarization $\boldsymbol{E}$ is parallel to the surface plane. The purpose of these measurement geometries is to enhance

higher-order diffraction relative to zeroth-order diffraction (forward scattering) in order to gain surface relaxation information; for details of the fundamental principles of *variable-polarization* scanned-angle-mode PhD, refer to references [57] and [58]. Scanned-angle measurements in the TM and TE geometries are achievable on the ALOISA beamline due to the possibility of rotating independently both the sample and electron analyser with respect to $\boldsymbol{E}$. In studying the $TiO_2(110)1 \times 1$ surface, Verdini *et al* recorded data from the O 1s and Ti 3s core-level features. Their analysis involved comparing experimental diffraction patterns, generated by calculating for each emission direction the ratio of the core-level intensities between the TM and TE geometries, to equivalent theoretically simulated data. They conclude that the surface is relaxed away from the bulk-terminated surface, and that their structure is consistent with that determined by SXRD [41] (see subsection 2.7). It should be noted that the primary objective of this study was to test the viability of *variable-polarization* scanned-angle-mode PhD for determining substrate surface relaxation, and that only a few structural parameters were optimized.

3. Forward look

Much of the work described above was carried out using second-generation synchrotron sources (more correctly storage rings). The increased brightness associated with third-generation sources has already been exploited to good effect in studies of oxide surfaces. This is particularly the case for SXRD measurements, where O positions are difficult to determine because of their relatively small x-ray scattering cross-section. There are many more opportunities to extend the knowledge base by tackling lower concentration and more complex systems that become tractable with the new sources. One area to highlight is the use of imaging methods. For example, developments in x-ray photoelectron microscopy (XPEEM) hold up the promise of spectroscopic measurements on a 20 Å diameter area [59]. This would provide a direct link with scanning probe methods and open up new vistas where, for instance, the behaviour of individual defects and supported metal clusters on oxides could be examined.

References

[1] Woodruff D P (ed) 2001 *Oxide Surfaces (The Chemical Physics of Solid Surfaces vol 9)* (Amsterdam: Elsevier)
[2] Feuerbacher B, Fitton B and Willis R F (ed) 1978 *Photoemission and the Electronic Properties of Surfaces* (New York: Wiley)
[3] Plummer E W and Eberhardt W 1982 *Advances in Chemical Physics* ed I Prigogone and S A Rice (New York: Wiley) pp 533–656
[4] Egelhoff W F Jr 1987 *Surf. Sci. Rep.* **6** 253
[5] Kevan S D (ed) 1992 *Angle Resolved Photoemission: Theory and Current Applications* (Amsterdam: Elsevier)
[6] Eberhardt W 1992 *Synchrotron Radiation Research (Advances in Surface and Interface Science vol 1)* ed R Z Bachrach (New York: Plenum) pp 139–97
[7] Flodström A, Nyholm R and Johansson B 1992 *Synchrotron Radiation Research (Advances in Surface and Interface Science vol 1)* ed R Z Bachrach (New York: Plenum) pp 199–251
[8] Mårtensson N and Nilsson A 1995 *Applications of Synchrotron Radiation, High-Resolution Studies of Molecules and Molecular Adsorbates on Surfaces* ed W Eberhardt (Berlin: Springer) pp 65–126
[9] Freund H-J and Kuhlenbeck H 1995 *Applications of Synchrotron Radiation, High-Resolution Studies of Molecules and Molecular Adsorbates on Surfaces* ed W Eberhardt (Berlin: Springer) pp 9–63
[10] Owen I W, Brookes N B, Richardson C H, Warburton D R, Quinn F M, Norman D and Thornton G 1986 *Surf. Sci.* **178** 897
[11] Brookes N B, Quinn F M and Thornton G 1987 *Solid State Commun.* **64** 383
[12] Wolfram W and Ellialtioglu S 1977 *Appl. Phys.* **13** 21
[13] Kaminski A, Mesot J, Fretwell H, Campuzano J C, Norman M R, Randeria M, Ding H, Sato T, Takahashi T, Mochiku T, Kadowaki K and Hoechst H 2000 *Phys. Rev. Lett.* **84** 1788

[14] Nozières P 1964 *Theory of Interacting Fermi Systems* (Reading, MA: Addison-Wesley)
[15] Davis L C 1986 *J. Appl. Phys.* **59** R25
[16] Prabhakaran K, Purdie D, Casanova R, Muryn C A, Hardman P J, Wincott P L and Thornton G 1992 *Phys. Rev.* B **45** 6969
[17] Warren S, Thomas A G, Hollingworth J, Flavell W R, Wincott P L, Prime A, Downes S and Chen Changkang 1997 *Surf. Sci.* **377–379** 256
[18] Eskes H, Tjeng L H and Sawatzky G A 1990 *Phys. Rev.* B **41** 288
[19] Segovia J L and Williams E M 2001 *Oxide Surfaces (The Chemical Physics of Solid Surfaces vol 9)* ed D P Woodruff (Amsterdam: Elsevier) pp 606–44
[20] Citrin P H 1986 *J. Physique Coll.* **47** C8 437
[21] Koningsberger D C and Prins R (ed) 1988 *X-ray Absorption: Principles, Applications, Techniques of EXAFS, SEXAFS, and XANES (Chemical Analysis vol 92)* (New York: Wiley)
[22] Muscat J, Harrison N M and Thornton G 1999 *Phys. Rev.* B **59** 15 457
[23] Gota S, Gautier-Soyer M, Douillard L, Durand J P and Le Fevre P 1996 *Surf. Sci.* **352–354** 1016
[24] Chun W-J, Asakura K and Iwasawa Y 1998 *Chem. Phys. Lett.* **288** 868
[25] Chun W-J, Asakura K and Iwasawa Y 1998 *J. Phys. Chem.* B **102** 9006
[26] Stöhr J 1992 *NEXAFS Spectroscopy (Springer Series in Surface Science vol 25)* ed R Gomer (Berlin: Springer)
[27] Lindsay R, Daniels B G and Thornton G 2001 *Oxide Surfaces (The Chemical Physics of Solid Surfaces vol 9)* ed D P Woodruff (Amsterdam: Elsevier) pp 199–255
[28] Lindsay R and Thornton G 2001 *Top. Catal.* at press
[29] Walsh J F, Davis R, Muryn C A, Thornton G, Dhanak V R and Prince K C 1993 *Phys. Rev.* B **48** 14 749
[30] Patthey L, Rensmo H, Persson P, Westermark K, Vayssieres L, Stashans A, Petersson A, Brühwiler P A, Siegbahn H, Lunell S and Mårtensson N 1999 *J. Chem. Phys.* **110** 5913
[31] Raza H, Harte S P, Muryn C A, Wincott P L, Thornton G, Casanova R and Rodriguez A 1996 *Surf. Sci.* **366** 519
[32] Zegenhagen J 1993 *Surf. Sci. Rep.* **18** 199
[33] Woodruff D P 1998 *Prog. Surf. Sci.* **57** 1
[34] Kendelewicz T, Liu P, Labiosa W B and Brown G E Jr 1995 *Physica* B **208/209** 441
[35] Liu P, Kendelewicz T, Nelson E J and Brown G E Jr 1998 *Surf. Sci.* **415** 156
[36] Liu P, Kendelewicz T, Nelson E J, Brown G E Jr and Parks G A 1998 *Surf. Sci.* **412/413** 287
[37] Zigan V F and Rothbauer R 1967 *Neues Jahrb. Mineral. Monatsh.* 137
[38] Vlieg E and Robinson I K 1992 *Synchrotron Radiation Crystallography* ed P Coppens (New York: Academic)
[39] Renaud G 1998 *Surf. Sci. Rep.* **32** 1
[40] Renaud G and Barbier A 2001 *Oxide Surfaces (The Chemical Physics of Solid Surfaces vol 9)* ed D P Woodruff (Amsterdam: Elsevier) pp 256–300
[41] Charlton G, Nicklin C L, Steadman P, Taylor J S G, Muryn C A, Harte S P, Mercer J, McGrath R, Norman D, Turner T S and Thornton G 1997 *Phys. Rev. Lett.* **78** 495
[42] Ramamoorthy M, Vanderbilt D and King-Smith R D 1994 *Phys. Rev.* B **49** 16 721
[43] Robach O, Renaud G and Barbier A 1998 *Surf. Sci.* **401** 227
[44] Masri P, Tasker P W, Hoare J P and Harding J H 1986 *Surf. Sci.* **173** 439
[45] Masri P and Tasker P W 1985 *Surf. Sci.* **149** 209
[46] Stoneham A M and Tasker P W 1998 *Surface and Near-Surface Chemistry of Oxide Materials* ed J Nowotny and L C Dufour (Amsterdam: Elsevier)
[47] Tasker P W 1988 *Adv. Ceram.* **10** 176
[48] Woodruff D P and Bradshaw A M 1994 *Rep. Prog. Phys.* **57** 1029
[49] Bradshaw A M and Woodruff D P 1995 *Applications of Synchrotron Radiation, High-Resolution Studies of Molecules and Molecular Adsorbates on Surfaces* ed W Eberhardt (Berlin: Springer) pp 127–69
[50] Chambers S A, Thevuthasan S, Kim Y J, Herman G S, Wang Z, Tober E, Ynzunza R, Morais J, Peden C H F, Ferris K and Fadley C S 1997 *Chem. Phys. Lett.* **267** 57
[51] Chambers S A, Henderson M A, Kim S J and Thevuthasan S 1998 *Surf. Rev. Lett.* **5** 381
[52] Thevuthasan S, Herman G S, Kim Y J, Chambers S A, Peden C H F, Wang Z, Ynzunza R X, Tober E D, Morais J and Fadley C S 1998 *Surf. Sci.* **401** 261
[53] Lindsay R, Baumgärtel P, Terborg R, Schaff O, Bradshaw A M and Woodruff D P 1999 *Surf. Sci.* **425** L401
[54] Polcik M, Lindsay R, Baumgärtel P, Terborg R, Schaff O, Bradshaw A M, Toomes R L and Woodruff D P 1999 *Faraday Discuss.* **114** 141
[55] Kuhlenbeck H, Odörfer, Illing G, Menges M, Mull Th, Freund H-J, Pöhlchen M, Staemmler V, Witzel S, Scharfshwerdt C, Wennemann K, Liedtke T and Neumann M 1991 *Phys. Rev.* B **43** 1969
[56] Pettersson L G M 1994 *Theor. Chim. Acta* **87** 293
[57] Verdini A, Sambi M, Bruno F, Cvetko D, Della Negra M, Gotter R, Floreano L, Morgante A, Rizzi G A and

Granozzi G 1999 *Surf. Rev. Lett.* **6** 1201
[58] Sambi M and Granozzi G 1998 *Surf. Sci.* **415** 1007
[59] Fink R, Weiss M R, Umbach E, Preikszas D, Rose H, Spehr R, Hartel P, Engel W, Degenhardt R, Wichtendahl R, Kuhlenbeck H, Erlebach W, Ihmann K, Schlogl R, Freund H-J, Bradshaw A M, Lilienkamp G, Schmidt T, Bauer E and Benner G 1997 *J. Electron Spectrosc. Relat. Phenom.* **84** 231